Intrinsic Selectivity and Structure Sensitivity of Rhodium Catalysts for C$_{2+}$ Oxygenate Production

Nuoya Yang,[∥,†] Andrew J. Medford,[∥,‡,§] Xinyan Liu,[‡,§] Felix Studt,[‡,§] Thomas Bligaard,[‡,§] Stacey F. Bent,[‡] and Jens K. Nørskov*[,‡,§]

†Department of Materials Science and Engineering, Stanford University, 496 Lomita Mall, Stanford, California 94305, United States
‡Department of Chemical Engineering, Stanford University, 443 Via Ortega, Stanford, California 94305, United States
§SLAC National Accelerator Laboratory, SUNCAT Center for Interface Science and Catalysis, 2575 Sand Hill Road, Menlo Park, California 94025, United States

Ⓢ Supporting Information

ABSTRACT: Synthesis gas (CO + H$_2$) conversion is a promising route to converting coal, natural gas, or biomass into synthetic liquid fuels. Rhodium has long been studied as it is the only elemental catalyst that has demonstrated selectivity to ethanol and other C$_{2+}$ oxygenates. However, the fundamentals of syngas conversion over rhodium are still debated. In this work a microkinetic model is developed for conversion of CO and H$_2$ into methane, ethanol, and acetaldehyde on the Rh (211) and (111) surfaces, chosen to describe steps and close-packed facets on catalyst particles. The model is based on DFT calculations using the BEEF-vdW functional. The mean-field kinetic model includes lateral adsorbate−adsorbate interactions, and the BEEF-vdW error estimation ensemble is used to propagate error from the DFT calculations to the predicted rates. The model shows the Rh(211) surface to be ∼6 orders of magnitude more active than the Rh(111) surface, but highly selective toward methane, while the Rh(111) surface is intrinsically selective toward acetaldehyde. A variety of Rh/SiO$_2$ catalysts are synthesized, tested for catalytic oxygenate production, and characterized using TEM. The experimental results indicate that the Rh(111) surface is intrinsically selective toward acetaldehyde, and a strong inverse correlation between catalytic activity and oxygenate selectivity is observed. Furthermore, iron impurities are shown to play a key role in modulating the selectivity of Rh/SiO$_2$ catalysts toward ethanol. The experimental observations are consistent with the structure-sensitivity predicted from theory. This work provides an improved atomic-scale understanding and new insight into the mechanism, active site, and intrinsic selectivity of syngas conversion over rhodium catalysts and may also guide rational design of alloy catalysts made from more abundant elements.
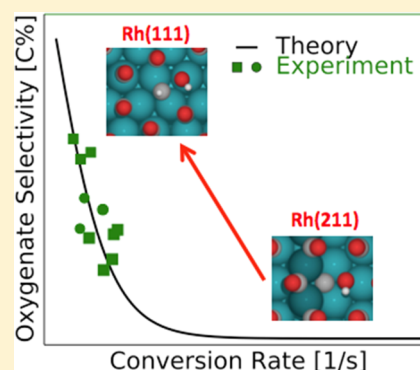
■ INTRODUCTION

Syngas conversion to higher oxygenates provides a promising pathway to transform coal, natural gas, and biomass into high value chemicals and transportation fuels.[1−3] However, development of catalysts with satisfactory activity and well-defined selectivity toward C$_{2+}$ oxygenates remains challenging[3−5] and hampers commercialization of this process. Rhodium (Rh) is often cited as the only elemental metal exhibiting some selectivity toward C$_{2+}$ oxygenates. Rh based catalysts have been studied extensively from both experimental and theoretical perspectives,[6−15] and the yield of ethanol and other C$_{2+}$ oxygenates has been considerably improved with appropriate choice of support and promoters.[2,12,16−19]

Interestingly, the selectivity patterns of pure Rh supported on silica vary significantly, and a fundamental understanding of how to achieve high selectivity is still limited. In some cases, "pure" Rh produces primarily methane and other light hydrocarbons,[10,12,20] while other studies show considerable selectivity toward C$_{2+}$ oxygenates.[11,13,21] In addition, it is still questionable if Rh is truly selective toward ethanol, as

significantly higher selectivity toward other C$_{2+}$ oxygenates, for example, acetaldehyde, is commonly reported.[22−25] Non-neman et al. found that the impurities in the support material, especially iron, were responsible for hydrogenating acetaldehyde into ethanol and that pure Rh is selective to acetaldehyde.[23,26] A recent report also shows a correlation between ethanol selectivity and various Rh−Fe alloy phases, while pure Rh is highly selective to methane.[27] Furthermore, support pretreatment[23,28] and particle size[29] also play critical roles in defining the selectivity of Rh catalysts. This varying performance of Rh-based catalysts indicates that there is ample room for improved understanding of the fundamental factors governing syngas conversion activity and selectivity.

In this work we hypothesize that the activity and selectivity of pure Rh catalysts is highly structure sensitive. With this hypothesis, the variation in syngas conversion across Rh catalysts can be explained by atomic-scale variations in the

structure of Rh catalyst particles. Structure sensitivity of Rh catalysts has been suggested previously,[7,8,30] but this hypothesis has not been described quantitatively. Herein we use density functional theory (DFT) calculations and microkinetic modeling to investigate the intrinsic selectivity toward methane, acetaldehyde and ethanol on the Rh(111) terrace and Rh(211) stepped surfaces in order to model the structure sensitivity of Rh catalysts. The theoretical results are then compared with experimental data collected on a variety of Rh catalysts. The calculations are performed using the recently developed BEEF-vdW functional[31] that has been shown to describe chemisorption energies on transition-metal surfaces particularly well, while at the same time including a description of dispersion forces.[32] In particular this functional has been shown to yield a quantitative description of surface energetics for larger adsorbates, e.g., those present in the hydrogenation of CO_2.[33,34] We also include lateral adsorbate−adsorbate interactions in order to yield a quantitative description of chemisorption energies under realistic conditions, and quantify the uncertainty of the exchange-correlation model and its propagation to macroscopic properties to assess the reliability of our conclusions.[35] Finally, a range of Rh catalysts supported on SiO_2 are tested experimentally for syngas conversion to provide a comparison to the theoretical results.

Our theoretical study finds the Rh(111) surface to be selective toward acetaldehyde, although a high C−O bond scission barrier limits the activity. In contrast, CO dissociation on the Rh(211) surface is more facile, resulting in higher activity but low selectivity to C_{2+} oxygenates. These findings are supported by the experimental observation that acetaldehyde and methane are the major products under differential reaction conditions, providing strong evidence that Rh catalysts are *intrinsically* selective toward acetaldehyde rather than ethanol. Moreover, we experimentally demonstrate that adding Fe or increasing CO conversion can increase the catalysts′ selectivity toward ethanol via subsequent hydrogenation of acetaldehyde. Furthermore, an inverse relation between the activity and C_{2+} oxygenates selectivity is experimentally observed, consistent with the trend expected from our theoretical model. These results indicate that close-packed surfaces are responsible for acetaldehyde production over Rh catalysts, while defect sites are significantly more active but selective toward methane. This improved atomic-scale understanding of Rh catalysts provides a framework for understanding activity and selectivity patterns of more complex Rh-based catalysts, and may have implications for the design and optimization of other catalytic systems for C_{2+} oxygenate production.

■ METHODS

Computational Methods. *Energy Calculations.* Electronic potential energies were calculated with density functional theory (DFT) performed with the Quantum ESPRESSO plane-wave code.[36] A plane-wave cutoff of 500 eV was used for all calculations and the Brillouin zone was sampled with a Monkhorst−Pack k-point grid.[37] Rhodium surfaces were modeled using slabs of varying size and thickness depending on the facet and intermediates, and a dipole correction was applied to all surfaces; all atomic structures are provided in the electronic Supporting Information. The Bayesian error estimation functional with van der Waals corrections, BEEF-vdW,[31] was employed, which includes a correction for van der Waals forces based on the vdW-DF2 functional.[38] The inclusion of vdW effects is particularly important for larger intermediates, such as the C_2 species in the acetaldehyde/ethanol synthesis pathway.[33,39,40] The BEEF-vdW

functional also provides uncertainties in the calculated exchange-correlation energies through error estimation ensembles.

Adsorption energies were calculated by optimizing the atomic geometries with a BFGS line search algorithm as implemented in the "atomic simulation environment" (ASE)[41] Python package. For small adsorbates a number of high-symmetry sites were tried and the minimal energy was used. For more complex adsorbates a number of initial guess geometries were generated using a minima-hopping algorithm[42] in conjunction with the HotBit DFTB calculator parametrized using BEEF-vdW calculations.[43] In the case of high CO* coverage the initial guess was generated by adding CO* adsorbates to the 3-fold sites which maximized the distance between the CO* and the coadsorbate. Transition-state geometries were calculated with the CI-NEB method[44] with an initial path generated by stretching the breaking bond from the most stable associated state. High-coverage transition-state paths were initialized based on the configuration of CO* that maximized the distance between the low-coverage transition-state and the CO* coadsorbates. All energies and further details can be found in the Supporting Information.

Vibrational frequencies were computed using a finite difference approximation to the Hessian and subsequent diagonalization to find the normal modes, as implemented in ASE.[41] Vibrational frequencies were used to compute the free energy of adsorbates by assuming that all degrees of freedom are harmonic vibrational modes. Imaginary and low frequency modes were replaced with a cutoff such that no mode contributes more than $3k_B$ to the entropy.[45] Gas-phase energies were computed with the BEEF-vdW functional and free energy corrections of gas-phase species were obtained using the Shomate equation[46] as implemented in CatMAP.[47]

Microkinetic Model. Microkinetic modeling was carried out using the CatMAP software package.[47] Site coverages are modeled using the mean-field approach and the steady-state approximation (i.e., the rate of change of all surface intermediate coverages is 0). The (111) surface is modeled using two surface sites: a "hydrogen reservoir" site,[5,48] and a site for all other intermediates. The (211) surface is modeled using three sites: a "fourfold" site corresponding to the quadruple-coordinated site at the base of the step, a step site corresponding to all other surface sites, and a hydrogen reservoir, in accordance with previous microkinetic models for ethanol synthesis.[5] The terrace site is omitted from the previous (211) model to provide a direct comparison between the kinetics on the (111) and (211) active sites. More details are provided in the Supporting Information.

Lateral adsorbate−adsorbate interactions were modeled using a second-order expansion in the coverage for the integral adsorption energy:

$$E_{int}(\theta_i) = \sum_i E_i^0 \theta_i + \frac{1}{2} \sum_s \sum_q f_{sq}^2 \sum_{i \in s} \sum_{j \in q} \varepsilon_{ij} \theta_i \theta_j \quad (1)$$

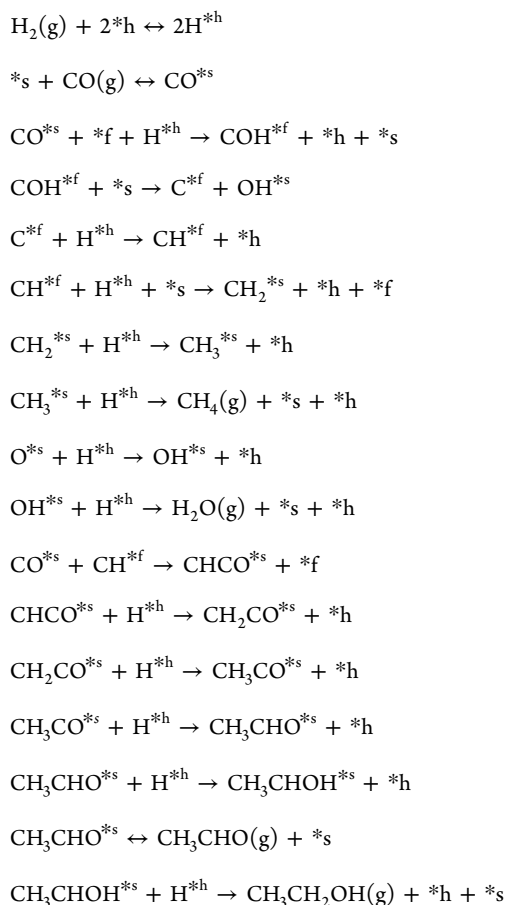from which the differential adsorption energy can be derived:

$$E_k = \frac{\partial E_{int}(\theta_i)}{\partial \theta_k}$$
$$= E_k^0 + \sum_s f_{sq_k}^2 \sum_{i \in s} \varepsilon_{ik} \theta_i + 2 \sum_s f_{sq_k} f'_{sq_k} \sum_{i \in s} \sum_{j \in q_k} \varepsilon_{ij} \theta_i \theta_j \quad (2)$$

where $E_{int}(\theta_i)$ is the integral adsorption energy of a surface given a vector of coverages θ_i, E_i^0 is the differential adsorption energy of species i in the low-coverage limit, ε_{ij} is a matrix of interaction parameters for the interaction between species i and j, f_{sq} corresponds to a piecewise-linear function for the energy as a function of coverage on sites s and q, and f'_{sq} is the derivative of this function with respect to the total coverage at sites s and q. Note that indicial notation is used so that an index that is not summed over corresponds to a vector; furthermore the shorthand notation $i \in s$ is used to denote all species i on site s, and q_k denotes the site q of species k. Further information on the interaction model is provided in the Supporting Information. On the basis of the strong CO* adsorption of Rh, it is expected that CO* will be the most abundant surface intermediate, and thus our model includes all interactions of surface intermediates with CO*. The CO*

cross-interaction parameters were determined using DFT calculations of the adsorption energies of intermediates at high CO* coverages, and the model was solved by first converging the solution with no interactions and incrementally increasing the interaction strength. Details regarding parametrization are provided in the Supporting Information.

Uncertainties associated with the exchange-correlation energies are provided by the BEEF-vdW ensemble. Since model inputs are chemisorption energies, the energetic errors are rescaled by a factor of 0.683; this reproduces the error associated with chemisorption energies rather than all properties used to fit the BEEF-vdW functional.[31,35] This uncertainty is propagated through the kinetic model by creating an ensemble of microkinetic models corresponding to the BEEF-vdW error estimation ensemble. This approach ensures that correlations between energetic errors are properly accounted for.[35] Uncertainties on rates were converged with an ensemble of 350 microkinetic models; more information is available in the Supporting Information.

The reaction mechanism for the (211) surface was inspired by previous work on ethanol synthesis over metal (211) facets.[5] The mechanism was simplified somewhat, keeping only the most important elementary steps:

$$H_2(g) + 2*h \leftrightarrow 2H^{*h}$$

$$*s + CO(g) \leftrightarrow CO^{*s}$$

$$CO^{*s} + *f + H^{*h} \rightarrow COH^{*f} + *h + *s$$

$$COH^{*f} + *s \rightarrow C^{*f} + OH^{*s}$$

$$C^{*f} + H^{*h} \rightarrow CH^{*f} + *h$$

$$CH^{*f} + H^{*h} + *s \rightarrow CH_2^{*s} + *h + *f$$

$$CH_2^{*s} + H^{*h} \rightarrow CH_3^{*s} + *h$$

$$CH_3^{*s} + H^{*h} \rightarrow CH_4(g) + *s + *h$$

$$O^{*s} + H^{*h} \rightarrow OH^{*s} + *h$$

$$OH^{*s} + H^{*h} \rightarrow H_2O(g) + *s + *h$$

$$CO^{*s} + CH^{*f} \rightarrow CHCO^{*s} + *f$$

$$CHCO^{*s} + H^{*h} \rightarrow CH_2CO^{*s} + *h$$

$$CH_2CO^{*s} + H^{*h} \rightarrow CH_3CO^{*s} + *h$$

$$CH_3CO^{*s} + H^{*h} \rightarrow CH_3CHO^{*s} + *h$$

$$CH_3CHO^{*s} + H^{*h} \rightarrow CH_3CHOH^{*s} + *h$$

$$CH_3CHO^{*s} \leftrightarrow CH_3CHO(g) + *s$$

$$CH_3CHOH^{*s} + H^{*h} \rightarrow CH_3CH_2OH(g) + *h + *s$$

where *s represents a "step site", *f represents a "four-fold site", and *h represents a "hydrogen reservoir" site. In summary, C–O bond scission occurs through the C–OH transition state, and C–CO coupling occurs via CH–CO. The C–OH transition-state was computed using both RPBE and BEEF-vdW functionals, and the similarity between transition-state energies and geometries indicates that the mechanism will be unaffected by the change in functional. The full set of elementary steps is provided in the Supporting Information. A similar model was used for the (111) surface, although the C–OH scission barrier was found to be prohibitively high (>2 eV). A number of C–O scission routes were explored and CH–OH scission was found to have the lowest transition-state energy. All other elementary steps were assumed to be the same as for the (211) surface.

Experimental Methods. In order to enlarge the variation of supported Rh catalysts, we developed a sample set in which we changed several variables in catalyst preparation, including the choice of the silica support and pretreatment, Rh precursor, as well as impregnation technique.

Support Pretreatment. Two types of silica gel were used as support: SiO_2-643 high purity grade, (Davisil grade 643, Sigma-Aldrich, surface area 300 m^2/g, 200–425 mesh) and SiO_2-60 (Alfa Aesar, surface area 500–600 m^2/g, 150–230 mesh). In some cases, the silica was washed in 2 M nitric acid aqueous solution under 353 K for 2 h, which are designated as SiO_2-643-washed or SiO_2-60-washed. Subsequently, the silica was centrifuged out and washed in deionized water to remove residual HNO_3. Then the silica was dried at 393 K in static air for 24 h. In other cases, silica was used as received, which are designated as SiO_2-643-unwashed or SiO_2-60-unwashed

Catalyst Preparation. The catalysts were prepared by incipient wetness impregnation (IWI). An appropriate amount of $RhCl_3 \cdot xH_2O$ (Sigma-Aldrich, 39 wt % Rh) or $Rh(NO_3)_3 \cdot xH_2O$ (Sigma-Aldrich, 36 wt % Rh) was dissolved in deionized water so that the Rh metal loading was 5 wt % and the solution volume equaled the total pore volume of the silica. IWI was applied in two ways, either under vacuum or at atmospheric pressure. In the former case, silica gel was added into a two-neck flask and evacuated. After isolating the system from vacuum pump, Rh solution was slowly injected into the flask while constantly stirring the silica. In the latter case, Rh solution was added into silica gel in a dropwise fashion while grinding the silica using pestle and mortar. After drying, the Rh catalysts were calcined in static air, at 773 K for 4 h. For preparation of the Fe promoted catalysts, a proper amount of $FeCl_3 \cdot 6H_2O$ (Sigma-Aldrich, 99% purity) was added into the Rh aqueous solution with an atomic ratio of either Rh/Fe = 100:1 or 1000:1; unwashed silica was used as the support and evacuation was applied during impregnation. Drying and calcination procedures were the same as undoped Rh catalysts.

Reaction Tests. Syngas conversion reactions were carried out in a tubular fixed bed reactor (glass-lined stainless steel, 30 cm length, 4 mm internal diameter). A gas purifier (Pall GASKLEEN ST) was used to remove nickel and iron carbonyl from CO before the gas stream enters the reactor. Usually, 100 mg catalyst was loaded into the reactor and reduced in situ at 523 K for 2 h in a H_2/He mixture (20 sccm H_2, 80 sccm He). After reduction, the pressure was increased to 20 bar while temperature remained at 523 K for the syngas conversion reaction. The total gas flow rate was 90 sccm and H_2/CO = 2. These flow rate and catalyst charge values were chosen to maintain CO conversion below 2% in order to measure intrinsic selectivity. All the products were analyzed in-line using gas chromatography (SRI 8610C) equipped with a capillary column and a HaysepD column, and the products were detected by two flame ionization detectors (FID). The selectivity was calculated on a carbon basis: $S_i = \frac{c_i r_i}{\sum_j c_j r_j}$ where c_i is the number of carbon atoms in species i and r_i is the production rate of species i. In this paper, C_{2+} oxygenates includes both acetaldehyde and ethanol, while other higher oxygenates were not detected in our syngas conversion reaction.

Catalyst Characterization. Rh nanoparticle size was analyzed by a FEI Tecnai G2 F20 X-TWIN transmission electron microscope (TEM) operated at 200 kV. Rh catalysts were reduced in 20%H_2/He at 523 K for 2 h before TEM characterization.

RESULTS AND DISCUSSION

Syngas Conversion on Rh(211). We start by investigating the activity and selectivity of the stepped Rh(211) surface in detail. It is well established that the CO dissociation energy on Rh(211) is substantially lower than that on Rh(111).[49] We also showed recently that Rh(211) is mainly selective to methane,[5] a finding that is based on density functional theory calculations employing the RPBE[50] functional and microkinetic modeling. Here we use results based on the BEEF-vdW functional in order to show that this finding is still valid when functionals

that include vdW interactions are used. We consider three different products that can be obtained by the hydrogenation of CO: methane, ethanol and acetaldehyde. We do this to model the main products usually found for Rh-based catalysts while keeping the reaction network in its most simple form (note that this network still consists of 15 intermediates and 14 barriers).

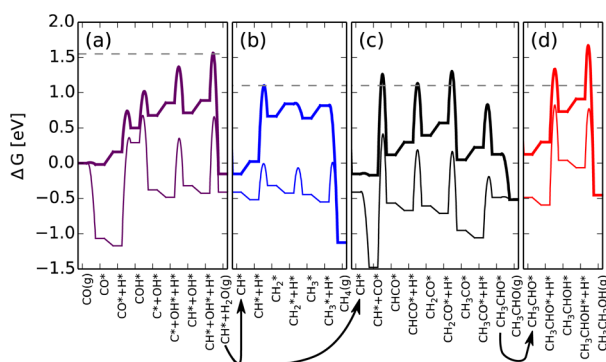The calculated free energy diagram toward these 3 products on the Rh(211) surface is shown in Figure 1. The free energy of

Figure 1. Free energy diagrams at 523 K on the Rh(211) surface without lateral adsorbate interactions (light line) and with lateral adsorbate interactions (bold line) at steady-state coverage. Panel (a) indicates the activity-limiting portion of the reaction pathway that is shared between all products. The dashed line indicates the activity-limiting barrier. Panel (b) shows the pathway unique to methane, while (c) shows the pathway unique to acetaldehyde, and (d) the pathway unique to ethanol. Dashed lines in panels (b–d) show the selectivity-liming transition-state, indicating selectivity toward methane. The species added at each step is labeled on the bottom axis. Free energies of reactants (CO, H_2) are computed at a pressure of 20 bar and H_2:CO = 2; all other free energies are computed at standard state.

CO adsorption energy at 523 K is calculated to be −0.98 eV indicating a high coverage of CO under realistic reaction conditions. Figure 2 shows the differential adsorption energy of CO on the step site as a function of coverage, indicating an equilibrium coverage of ∼0.7 ML of CO. Figure 2 also indicates that the adsorbate−adsorbate interaction model provides a good description of the coverage-dependent adsorption energy since the error between the model (line) and DFT calculations (points) is typically less than 0.2 eV. The change of the free energy landscape upon inclusion of adsorbate−adsorbate interactions between all intermediates and transition-states and coadsorbed CO* is shown in Figure 1 (bold lines). It can be seen that the energies of intermediates and transition-states are substantially shifted up in energy. Scission of the CO bond via the C−OH intermediate has a free energy barrier of 1.38 eV from the gas-phase, indicating high rates of CO hydrogenation (Figure 1a). As can be seen by comparison of the subsequent barriers for methane, ethanol and acetaldehyde formation in Figures 1b−d, the Rh(211) surface will likely be selective toward methane as the main product. All CH_x hydrogenation barriers are lower in free energy than the $H−CH_3CO$ hydrogenation barrier that appears to be the rate-limiting step for the formation of both acetaldehyde and ethanol.

Figure 3 shows the outcome of the microkinetic model at differential reaction conditions and is consistent with the observations obtained from the free energy diagram. Figure 3a shows the logarithm of the rate as a function of temperature. The rate of CO hydrogenation to methane is about 0.01 turnover/s at 525 K while the rates for ethanol and
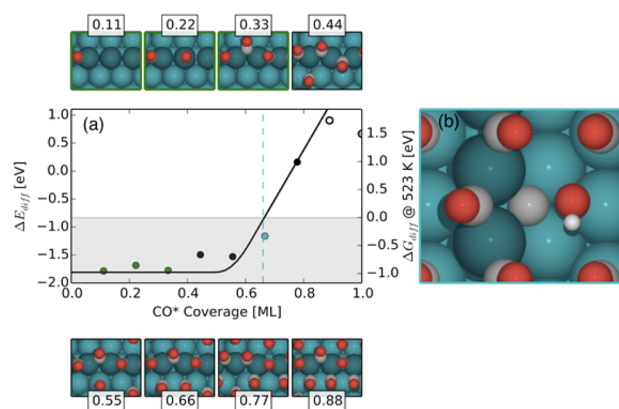

Figure 2. (a) Coverage-dependent differential binding energies for CO adsorption on the Rh(211) surface. Images on the top/bottom depict the spatial configuration of CO* adsorbates as a function of coverage. Black circles represent energies computed using DFT and the solid line corresponds to the adsorbate−adsorbate interaction model. Solid circles were used in the parametrization, while hollow circles are shown for reference. The green points correspond to adsorption at step boundary atoms (darker in images), and the cyan circle corresponds to the total coverage used for cross-interaction parametrizations. Differential binding energies are estimated as $E_{\mathrm{diff}}(\theta) = \frac{E_{\mathrm{int}}(\theta) - E_{\mathrm{int}}(\theta - 0.11)}{0.11}$ for DFT calculations and the adsorbate interaction model (where 0.11 represents the finite $\Delta\theta$ of DFT calculations). The shaded region indicates an exergonic adsorption at 523 K. (b) C−OH transition-state at high CO* coverage. Cross-interactions were parametrized at a total coverage of 0.66 ML as indicated by the cyan point and dashed line.

acetaldehyde are orders of magnitude lower (∼10^{-18} and ∼10^{-3} at 525 K, respectively). The BEEF-vdW error estimation ensemble was used to analyze the implications of exchange-correlation uncertainty on the predicted rates and selectivities. The error bars in Figure 3a indicate that the uncertainty on absolute magnitude of turnover frequency is ∼1−2 orders of magnitude; however, there is a significant difference of ∼2 orders of magnitude between the turnover frequency of methane and acetaldehyde at 525 K. Figure 3b shows the selectivities for each product with associated error bars estimated from the BEEF-vdW ensemble. Even with exchange-correlation uncertainty, the Rh(211) facet is predicted to be >90% selective to methane. The fact that the turnover frequency for ethanol is even lower by ∼15 orders of magnitude indicates that the Rh(211) facet is unlikely to produce C_{2+} oxygenates as a major product at typical reaction conditions.

Syngas Conversion on Rh(111). As shown above, we established that the Rh(211) surface exhibits low selectivity to C_{2+} oxygenates and mainly produces methane. While methane is the main product for a variety of Rh-based catalysts,[10,12,20] it is well established that there are a large number of Rh catalysts that produce C_{2+} oxygenates. We therefore hypothesize that other, less reactive, facets are responsible for C_{2+} oxygenates selectivity. We chose to investigate the close-packed Rh(111) facet as this facet is usually the least reactive on transition metal surfaces.

The free energy diagram of CO hydrogenation to methane, ethanol and acetaldehyde on the Rh(111) surface is shown in Figure 4, with and without explicit inclusion of adsorbate− adsorbate interactions. We calculate the adsorption of CO* at low coverage (1/4 ML) to be −1.6 eV in good agreement with
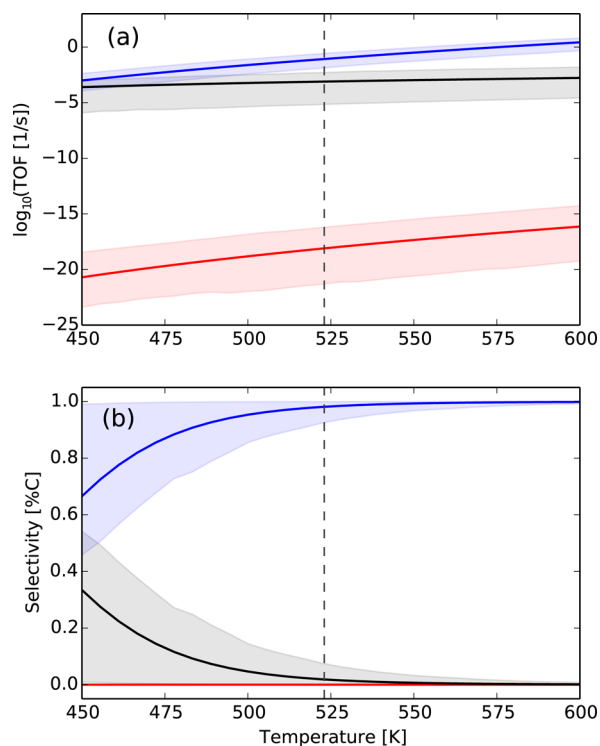
Figure 3. (a) Turnover frequencies and (b) carbon selectivities for methane (blue), acetaldehyde (black) and ethanol (red) calculated using the microkinetic model for Rh(211). Error bars correspond to the 84th and 16th percentile of the kinetic model distribution computed using energies from the BEEF-vdW error ensemble. The reaction conditions are $p_{H_2} = 6.66$, $p_{CO} = 13.33$, $p_{H_2O} = p_{CH_4} = p_{AcH} = p_{EtOH} \approx 0$ bar. Vertical gray dashed line marks the experimental conditions of this work (523 K).
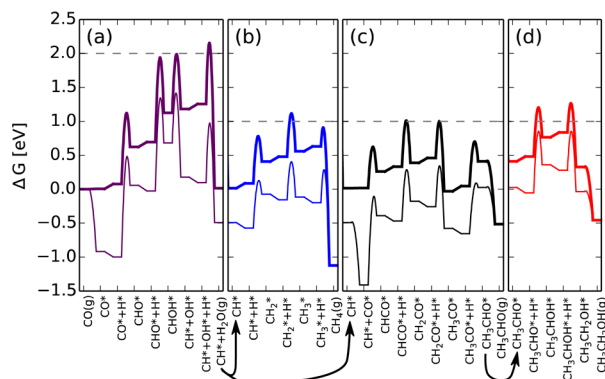
Figure 4. Free energy diagrams at 523 K on the Rh(111) surface without lateral adsorbate interactions (light line) and with lateral adsorbate interactions (bold line) at steady-state coverage. Panel (a) indicates the activity-limiting portion of the reaction pathway that is shared between all products. The dashed line indicates the activity-limiting barrier. Panel (b) shows the pathway unique to methane, while (c) shows the pathway unique to acetaldehyde, and (d) the pathway unique to ethanol. Dashed lines in panels (b−d) show the selectivity-liming transition-state, indicating selectivity toward methane. The species added at each step is labeled on the bottom axis. Free energies of reactants (CO, H_2) are computed at a pressure of 20 bar and H_2:CO = 2; all other free energies are computed at standard state.

the experimental value (−1.5 eV).[32] Figure 5 shows that this adsorption energy is decreased at higher coverages, leading to an equilibrium coverage of ∼0.55 ML CO at 14 bar CO and T
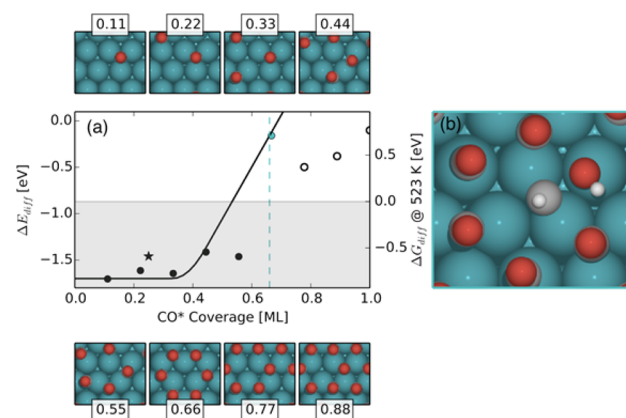

Figure 5. (a) Coverage-dependent differential binding energies for CO adsorption on the Rh(111) surface. Images on the top/bottom depict the spatial configuration of CO* adsorbates as a function of coverage. Black circles represent energies computed using DFT, the black star corresponds to the experimental value,[32] and the solid line corresponds to the adsorbate−adsorbate interaction model. Solid circles were used in the parametrization, while hollow circles are shown for reference, and the cyan circle corresponds to the total coverage used for cross-interaction parametrizations. Differential binding energies are estimated as $E_{diff}(\theta) = \frac{E_{int}(\theta) - E_{int}(\theta - 0.11)}{0.11}$ for DFT calculations and the adsorbate interaction model. The shaded region indicates an exergonic adsorption at 523 K. (b) CH−OH transition-state at high CO* coverage. Cross-interactions were parametrized at a total coverage of 0.66 ML as indicated by the cyan point and dashed line.

= 523 K when adsorbate−adsorbate interactions are considered. All other intermediates are calculated to experience adsorbate−adsorbate interactions with coadsorbed CO* at a coverage of 0.55 ML CO and the binding energies of intermediates and transition states are decreased by 0.1 to 1 eV as seen in Figure 4b−d. The coverage-dependent model in Figure 5 overestimates the effect of adsorbate−adsorbate interactions, particularly at high coverages, indicated by the fact that the model (solid line) predicts significantly higher energies than DFT (circles) at CO* coverages greater than 0.66 ML. The system seems to exhibit a phase transition around 2/3 ML, a phenomenon that is not captured by the piecewise linear model used to parametrize coverage dependence. However, the model is relatively accurate in the regions of interest and represents a good first step toward quantification of lateral adsorbate−adsorbate interactions.

Direct C−O bond scission on (111) surfaces is known to exhibit a rather high barrier[49] and we find that the most likely mechanism proceeds via splitting of the C−O bond in the CHOH intermediate; CH* can than be hydrogenated further to yield methane. Adsorbed CH* can alternatively couple with CO* to create a CHCO* backbone that can be hydrogenated to either ethanol or acetaldehyde. Inspection of the overall energetics of the free energy diagram in Figure 4 indicates a close competition between the hydrogenation of CH_2* and CH_2CO* as the selectivity-determining step. It is, however, rather difficult to make predictions about selectivity from the free energy diagram alone and we will again investigate the activity and selectivity using a microkinetic model. As discussed for Rh(211) this model explicitly includes the effect of adsorbate−adsorbate interactions at the estimated coverage of CO of 0.55 ML.

The calculated turnover frequencies for the production of methane, ethanol and acetaldehyde are shown in Figure 6a along with the corresponding selectivities in Figure 6b. As can be seen, methane and acetaldehyde production are calculated to be 10^{-8} and $10^{-7} s^{-1}$ at 525 K, while ethanol is produced at a very low rate ($10^{-15} s^{-1}$ at 525 K). At 525 K acetaldehyde is
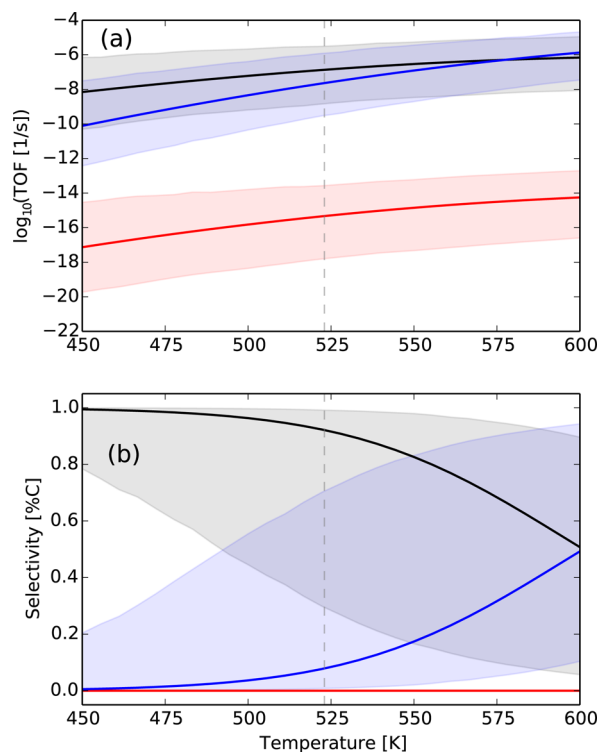

Figure 6. (a) Turnover frequencies and (b) carbon selectivities for methane (blue), acetaldehyde (black), and ethanol (red) calculated using the microkinetic model for Rh(111). Error bars correspond to the 84th and 16th percentile of the kinetic model distribution computed using energies from the BEEF-vdW error ensemble. The reaction conditions are $p_{H_2} = 6.66$, $p_{CO} = 13.33$. $p_{H_2O} = p_{CH_4} = p_{AcH} = p_{EtOH} \approx 0$ bar. Vertical gray dashed line marks the experimental conditions of this work (523 K).

therefore predicted to be the main product on Rh(111) and methane only becomes more favorable at higher temperatures. It should be noted here that the rate of methane is decreased by ~8 orders of magnitude between Rh(211) and Rh(111), a fact that is supported by experiments.[49] These findings suggest high acetaldehyde selectivity on Rh(111) at 523 K. The relatively large uncertainty of the results makes it rather difficult to precisely determine the selectivity at high temperatures. Even with this uncertainty, however, the acetaldehyde selectivity is nearly always predicted to be greater than zero, and is substantially higher than the oxygenate selectivity predicted for the Rh(211) surface in Figure 3b.

Although the results indicate that the Rh(111) surface will be more selective toward C_{2+} oxygenates in general, it is worth noting the extremely low turnover frequencies for ethanol production. Rhodium has often been reported to produce ethanol with reasonably high selectivity,[13,17,18] although there are a number of other reports in which it was observed to produce primarily methane and acetaldehyde,[10,22,24]. In order to more systematically understand the experimental selectivity pattern between ethanol and acetaldehyde production on Rh catalysts, the selectivity was measured experimentally for a number of SiO_2 supported Rh catalysts. As discussed in the following section, the experimental results show methane and acetaldehyde as the primary products, fully consistent with our theoretical analysis.

Another result of the microkinetic model of the Rh(111) surface is the relatively low turnover frequencies for the formation of all products. The total consumption rate at 523 K is on the order of 10^{-7} s^{-1}, considerably lower than experimentally measured turnover frequencies of ~$10^{-4}-10^{-2}$ s^{-1} in this or other work,[12,29] even when the uncertainty of the exchange-correlation approximation is included. This low rate is consistent with the overall barrier of ~2 eV for both CHO-H hydrogenation and CH−OH bond scission at steady state. One possibility is that C−O bond scission occurs through some other pathway, but numerous routes were explored and the CH−OH bond scission barrier was found to be significantly lower than that of other alternatives. Another possibility is that the interaction model overestimates the destabilization of intermediates and transition-states at high CO* coverage, since

Table 1. Catalytic Activity and Selectivity of Various Rh Catalysts[a]

sample number	Rh precursor	type of silica	impregnation method	CO conversion (%)	s(CH_4) %	s(C_{2+}HC) %	s(AcH)[b] %	s(EtOH)[b] %	s(total C_{2+}oxy) %
1	RhCl_3	Davisil 643; unwashed	vacuum	0.36	29.29	5.68	60.32	2.02	62.33
2	RhCl_3	Davisil 643; unwashed	vacuum	0.68	36.15	4.63	51.42	6.80	58.22
3	RhCl_3	Davisil 643; unwashed	vacuum	0.47	29.02	13.92	52.44	3.74	56.18
4	RhCl_3	Davisil 643; washed	vacuum	1.56	50.71	14.28	29.38	3.47	33.45
5	RhCl_3	Davisil 643; washed	vacuum	1.79	53.78	9.70	31.65	3.17	34.81
6	RhCl_3	Davisil 643; washed	vacuum	1.08	46.66	28.99	19.44	2.59	22.63
7	RhCl_3	Davisil 643; washed	grinding	1.48	45.33	28.18	24.94	0.00	25.90
8	RhCl_3	SiO_2-60; unwashed	vacuum	0.54	42.47	6.56	42.86	1.53	44.39
9	RhCl_3	SiO_2-60; washed	vacuum	1.05	48.83	9.24	40.41	0.50	40.91
10	Rh(NO_3)_3	SiO_2-60; unwashed	grinding	0.46	43.62	16.59	35.14	0.00	35.14
11	Rh(NO_3)_3	Davisil-643; washed	grinding	0.64	50.44	14.87	32.34	0.00	32.34

[a]Methanol and CO_2 have been produced from some catalysts with very low selectivity. A table including selectivity to all measured products is included in the Supporting Information (section 5.1). Conversion can be converted to rate using the factor 1% conversion = 2.225 μmol/gcat·s. Catalyst: 0.1 g; reaction conditions: T = 523 K, P = 20 bar, flow rate 90 sccm (H_2/CO = 2). [b]AcH = acetaldehyde; EtOH = ethanol.

the finite cells used to model the surface cannot account for long-range order/disorder and the mean-field model does not contain information about local configurations.[51] A final possibility is that C−O bond scission occurs primarily at sites other than the clean (111) surface, such as alkali impurities or on step defects similar to the Rh(211) surface where the C−O bond scission rate is much faster, and CH_x^* intermediates diffuse to terrace sites where they can be selectively converted to C_{2+} oxygenates. This scenario is considered in more detail in the following sections.

Experimental Oxygenate Selectivity. In order to obtain a more systematic understanding of the selectivity patterns for Rh catalysts, a number of Rh/SiO_2 catalysts were tested experimentally. Synthesis methods were varied to build up a Rh catalyst sample set exhibiting a range of catalytic activities and selectivities. Methane and acetaldehyde were the major products found for all Rh catalysts tested, although a wide range of overall activity and C_{2+} oxygenates selectivity were observed. A detailed table of the activity and selectivity of various Rh catalysts tested in this study is given in Table 1. Washed and unwashed silica supports without the presence of Rh were also tested and no syngas conversion activity was detected (data included in Supporting Information section 5.1).

Although the selectivity toward total C_{2+} oxygenates varies substantially among different catalysts, acetaldehyde is always the major C_{2+} oxygenate species. The molar ratio between ethanol and acetaldehyde is below 0.2 for all the Rh catalysts tested, as is shown in Figure 7a. This low ratio supports the calculated free energy diagrams, Figure 1 and 4 whereby
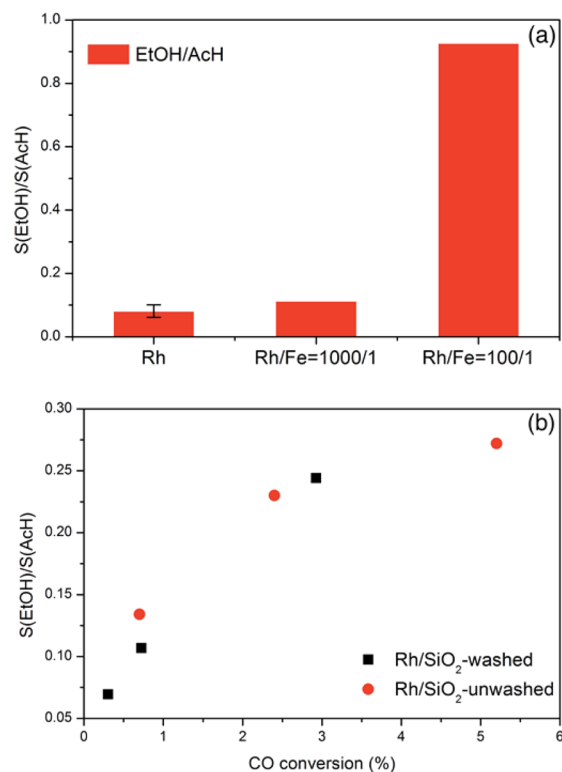

reduction of acetaldehyde to ethanol on Rh(211) and Rh(111) has a rather high energy barrier of ∼2 eV at steady-state. However, some previous experimental studies reported higher ethanol selectivity than acetaldehyde.[11,12,17,21] The presence of impurities and extent of CO conversion are among the possible explanations for this contradiction and we demonstrate that the ratio between ethanol and acetaldehyde can be increased by introducing small amount of Fe or operating under higher CO conversion.

Fe has been identified as an effective promoter for ethanol synthesis from Rh based catalysts.[10,23,27] To demonstrate the effect of potential Fe impurities, we purposely promoted the Rh catalysts with small amounts of Fe. As shown in Figure 7a, catalysts with an atomic ratio of Rh/Fe = 100/1 show significantly enhanced selectivity toward ethanol, although total C_{2+} oxygenate selectivity remains similar to the unpromoted Rh counterparts (data not shown here, see Supporting Information section 5.2). This observation is consistent with previous work by Nonneman et al.,[23] who observed a similar effect even at significantly lower Fe concentrations. We note that Fe is a relatively ubiquitous impurity, and it is plausible that the Rh catalysts in some previous studies may have had sufficiently high Fe concentrations to drive the selectivity distribution toward ethanol. Although a detailed explanation of this phenomenon is outside the scope of this work, we hypothesize that Fe−Rh sites could facilitate faster hydrogenation of acetaldehyde to ethanol.

Another possible explanation for higher ethanol/acetaldehyde ratios lies in the fact that ethanol is more thermodynamically stable than acetaldehyde at temperatures below 540 K.[44] This implies that higher CO conversion will facilitate hydrogenation of acetaldehyde into ethanol. We tested two representative Rh catalysts under different CO conversion, and a higher ratio between ethanol and acetaldehyde was achieved with increasing CO conversion (Figure 7b). This effect may play an important role in supported catalysts even at a relatively low overall conversion, since the local concentration at the catalyst surface will depend on the porosity and diffusion characteristics of the support material.

Ultimately the ratio between ethanol and acetaldehyde will be a complex function of the impurities present in a catalyst or its support, the overall conversion, and the local concentration gradients within the catalyst support. Current theoretical methods make quantitative modeling of such a complex system prohibitive; however, the results of microkinetic modeling at differential conditions along with the consistent findings for a set of Rh/SiO_2 catalysts at low conversion provide strong evidence that Rh is *intrinsically* selective toward acetaldehyde rather than ethanol.

Activity vs Selectivity Relationship. The results of the microkinetic models in Figures 3 and 6 indicate that the Rh(211) surface is much more active than the Rh(111) surface, while the Rh(111) surface is more selective toward C_{2+} oxygenates. Any real catalyst will have some distribution of (111)-like close-packed facets and (211)-like step and kink defects, thus the overall activity and selectivity will have contributions from both active sites. This could explain the large variance that is usually observed in the activity and selectivity of Rh catalysts[11,13,21−24] since the active site distribution will be influenced by numerous factors in the synthesis of a catalytic sample.

This hypothesis leads to the prediction that there should be an inverse correlation between catalytic activity and selectivity if

Figure 7. (a) The ratio between the selectivity toward ethanol (EtOH) and acetaldehyde (AcH) for unpromoted and Fe-promoted Rh catalysts, at the Rh/Fe ratios indicated. Unwashed SiO_2 Davisil 643 was used as the support. (b) The selectivity ratio as a function of CO conversion for both washed and unwashed Rh/SiO_2 catalysts. The experimental conditions are given in Table 1.

the terrace sites are selective but inactive, and the defect sites are active but not selective. In order to quantify this effect, a simple linear combination of rate ensembles from the Rh(111) and Rh(211) surfaces was used to simulate the effect of varying the concentration of Rh(211) step sites from 0 to 100%. In reality the two sites will be coupled via diffusion, and the spatial configuration may also play an important role; however, the linear combination approach provides a quantitative illustration of the change in rate and selectivity as the active site distribution changes. The results, shown in Figure 8 clearly demonstrate an inverse correlation between activity and C_{2+} oxygenate selectivity.
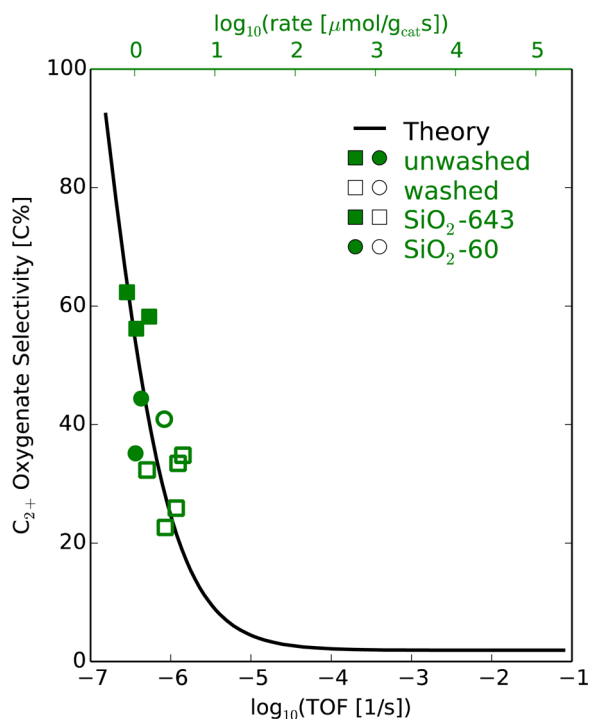

Figure 8. Correlation between activity and the selectivity toward total C_{2+} oxygenates obtained at 523 K. Theory line is obtained using a linear combination of rates from the Rh(211) and Rh(111) microkinetic model ensembles and is plotted on the lower axis. Points correspond to experimental measurements on Rh/SiO$_2$ catalysts and are plotted on the upper axis (filled = washed, unfilled = unwashed, square = SiO$_2$-643, circle = SiO$_2$-60). The conditions for the microkinetic model are the same as Figure 3 and 6, and experimental conditions are the same as Table 1.

The predicted inverse correlation was also observed experimentally. Figure 8 shows the correlation between activity and C_{2+} oxygenate selectivity for the various Rh/SiO$_2$ catalysts, with each data point representing one catalyst. A clear trend of decreasing C_{2+} oxygenate selectivity with increasing activity is observed. Although the agreement with the kinetic model is only semiquantitative, the observation provides strong support for the structure-sensitive hypothesis.

We note that the more active catalysts will also have higher conversion since the flow rate was held constant between samples. Given that methane is the thermodynamically favorable product, this may also explain the decrease in C_{2+} oxygenate selectivity. However, the ratio between the selectivity of C_{2+} oxygenates and methane remains stable over different CO conversion (see Supporting Information Figure 4),

indicating that the inverse activity-selectivity correlation is related to the kinetics of the process.

Obtaining direct characterization of the surface site structure of supported nanoparticles is challenging. For future studies, aberration-corrected TEM and sulfur titration techniques may provide direct evidence on the surface site distribution of supported Rh catalysts.

On the basis of the catalysts tested in this study, we note that the difference in selectivity patterns can be primarily attributed to support pretreatment. Rh supported on unwashed silica usually exhibits lower activity and a selectivity of ~60% toward C_{2+} oxygenates and ~30% toward methane; the selectivity pattern is reversed for Rh supported on washed silica but the activity is usually higher. On the basis of the hypothesis outlined above, this implies that the unwashed sample has a larger ratio of terrace/step sites. The variation could arise due to different particle size distributions on the washed vs. unwashed supports. To investigate this we measured the size of the particles using TEM. The results indicate that the average particle size and size distribution are similar between washed and unwashed samples: 3.36 ± 1.52 nm washed vs. 3.25 ± 1.37 nm unwashed (see Supporting Information section 5.4 for details). However, extremely small or very large particles tend to be overlooked in TEM characterization. In addition, the shapes and concentration of defect sites could still be influenced by the support surface properties, leaving open the possibility that the washed sample could produce more step and defect sites.

Another possibility is that the active site distribution is affected by impurities in the support, as the impurities in the unwashed silica can dissolve into the impregnation solution[23] or migrate via surface diffusion and be preferentially located at the step and kink sites of the Rh nanoparticles.[52−54] Thus, the effective percentage of step and kink sites of Rh supported on unwashed silica may be lowered due to blockage from impurities. Such physical blockage of defect sites has been previously proposed[55−57] and alkali metals or metal oxides were also suggested to block active sites for CO dissociative adsorption on non-noble metal-based syngas conversion catalysts.[53,58] Alkali metals have also been commonly used as promoters for Rh catalysts to enhance selectivity to higher oxygenates, although the activity is usually decreased.[20,55,57−60] As sodium is the highest concentration impurity in silica, we hypothesize that small amounts of sodium may play an important role in modulating the active site distribution. Future work will focus on testing the hypothesis of the role of alkali metals in controlling active site distributions.

■ CONCLUSIONS

The activity and selectivity of Rh(211) and Rh(111) surfaces for conversion of CO and H$_2$ into methane, acetaldehyde, and ethanol have been investigated by DFT calculations that include vdW interactions. The pathways toward the different products have been calculated at relevant CO coverages thus explicitly accounting for adsorbate−adsorbate interactions. These energetics were used to establish microkinetic models of these reactions on the two different surfaces that also address the uncertainty of our results. It is found that the selectivity toward C_{2+} oxygenates is strongly structure dependent, with (211) surfaces selective toward methane and (111) surfaces selective toward acetaldehyde. This is mainly due to the fact that the activity toward methane on the (211) surfaces is much higher due to significantly lower C−O bond scission barriers,

whereas the rates for acetaldehyde and ethanol are comparable on both surfaces. These conclusions were found to be robust to the exchange-correlation approximation using the BEEF-vdW error estimation ensembles.

The results of the microkinetic models also indicate a strong kinetic preference toward acetaldehyde rather than ethanol for both Rh(211) and Rh(111) surfaces when considering differential reaction conditions. A number of Rh/SiO$_2$ catalysts were synthesized and tested experimentally at low conversion, and acetaldehyde was observed as the primary oxygenate product for all samples, consistent with the theoretical results. The presence of Fe impurities and higher overall conversion are shown to increase the ethanol/acetaldehyde ratio, but at low conversion both the theoretical models and experimental results support the conclusion that Rh catalysts are intrinsically selective toward acetaldehyde.

The implications of structure sensitivity were explored by considering the fact that a real catalyst will contain both (111)-like and (211)-like sites. The natural variation in active site distribution is proposed as an explanation for the variance in catalytic activity and selectivity reported in the literature even for catalysts that are nominally the same. An inverse correlation between catalytic activity and selectivity is predicted by the model and also observed experimentally in a series of Rh/SiO$_2$ samples investigated in this work, providing further support for the hypothesis.

The findings in this work provide fundamental insight into of the activity and selectivity patterns of Rh catalysts for C$_{2+}$ oxygenate production, and the concept of structure sensitivity supplies a quantitative explanation for the inherent variation in catalytic performance and the activity/selectivity trade-off. This understanding provides a necessary first step toward the optimization of Rh catalysts for syngas conversion, and suggests a new strategy for the design of new catalysts for C$_{2+}$ oxygenate synthesis.

■ ASSOCIATED CONTENT

Ⓢ Supporting Information

The Supporting Information is available free of charge on the ACS Publications website at DOI: 10.1021/jacs.5b12087.

> Density functional theory calculations; lateral adsorbate interaction model; microkinetic modeling; activity and selectivity of Fe doped catalysts; selectivity under varying CO conversions; TEM characterization. (PDF)
> Atomic structures for all adsorbates and transition-states on Rh(111) surface (XYZ)
> Atomic structures for all adsorbates and transition-states on Rh(211) surface (XYZ)

■ AUTHOR INFORMATION

Corresponding Author

*norskov@stanford.edu

Author Contributions

‖N.Y. and A.J.M. contributed equally.

Notes

The authors declare no competing financial interest.

■ ACKNOWLEDGMENTS

■ REFERENCES

(1) Spivey, J. J.; Egbebi, A. *Chem. Soc. Rev.* **2007**, *36* (9), 1514−1528.
(2) Subramani, V.; Gangwal, S. K. *Energy Fuels* **2008**, *22* (2), 814−839.
(3) Mohanty, P.; Pant, K. K.; Naik, S. N.; Parikh, J.; Hornung, A.; Sahu, J. N. *Renewable Sustainable Energy Rev.* **2014**, *38*, 131−153.
(4) Gerber, M. A.; White, J. F.; Stevens, D. J. *Mixed Alcohol Synthesis Catalyst Screening 2007 Progress Report; Formal Report to DOE*, 2007; No. PNNL-16763.
(5) Medford, A. J.; Lausche, A. C.; Abild-Pedersen, F.; Temel, B.; Schjødt, N. C.; Nørskov, J. K.; Studt, F. *Top. Catal.* **2014**, *57* (1−4), 135−142.
(6) Choi, Y.; Liu, P. *J. Am. Chem. Soc.* **2009**, *131* (36), 13054−13061.
(7) Kapur, N.; Hyun, J.; Shan, B.; Nicholas, J. B.; Cho, K. *J. Phys. Chem. C* **2010**, *114*, 10171−10182.
(8) Wang, J.; Liu, Z.; Zhang, R.; Wang, B. *J. Phys. Chem. C* **2014**, *118* (211), 22691−22701.
(9) Burch, R.; Petch, M. I. I. *Appl. Catal., A* **1992**, *88* (1), 39−60.
(10) Haider, M.; Gogate, M.; Davis, R. *J. Catal.* **2009**, *261* (1), 9−16.
(11) Subramanian, N. D.; Gao, J.; Mo, X.; Goodwin, J. G.; Torres, W.; Spivey, J. J. *J. Catal.* **2010**, *272* (2), 204−209.
(12) Yu-hua, D.; De-An, C.; Khi-Rui, T. *Appl. Catal.* **1987**, *35* (1), 77−92.
(13) Yin, H.; Ding, Y.; Luo, H.; Zhu, H.; He, D.; Xiong, J.; Lin, L. *Appl. Catal., A* **2003**, *243* (1), 155−164.
(14) Huang, Y.; Deng, W.; Guo, E.; Chung, P.-W.; Chen, S.; Trewyn, B. G.; Brown, R. C.; Lin, V. S.-Y. *ChemCatChem* **2012**, *4* (5), 674−680.
(15) Filot, I. A. W.; Broos, R. J. P.; van Rijn, J. P. M.; van Heugten, G. J. H. A.; van Santen, R. A.; Hensen, E. J. M. *ACS Catal.* **2015**, *5*, 5453−5467.
(16) Pan, X.; Fan, Z.; Chen, W.; Ding, Y.; Luo, H.; Bao, X. *Nat. Mater.* **2007**, *6* (7), 507−511.
(17) Wang, J.; Zhang, Q.; Wang, Y. *Catal. Today* **2011**, *171* (1), 257−265.
(18) Gao, J.; Mo, X.; Goodwin, J. G. *J. Catal.* **2009**, *268* (1), 142−149.
(19) Martin, A.; Lücke, B.; Jaeger, N. J.; Schulz-Ekloff, G.; Gutschick, D.; Miessner, H. *Catal. Lett.* **1992**, *13* (3), 247−259.
(20) Mo, X.; Gao, J.; Goodwin, J. G., Jr. *Catal. Today* **2009**, *147* (2), 139−149.
(21) Liu, Y.; Murata, K.; Inaba, M.; Takahara, I.; Okabe, K. *Catal. Today* **2011**, *164* (1), 308−314.
(22) Gerber, M. A.; Gray, M. J.; Stevens, D. J.; White, J. F.; Thompson, B. L. *Optimization of Rhodium-Based Catalysts for Mixed Alcohol Synthesis 2009 Progress Report; Formal Report to DOE*, 2010, PNNL-20115.
(23) Nonneman, L. E. Y.; Bastein, A. G. T. M.; Ponec, V.; Burch, R. *Appl. Catal.* **1990**, *62* (1), 23−28.
(24) Jiang, D.; Ding, Y.; Pan, Z.; Chen, W.; Luo, H. *Catal. Lett.* **2008**, *121* (3−4), 241−246.
(25) *Progress in C1 Chemistry in Japan*; Kodansha: Tokyo, 1989.
(26) Burch, R.; Petch, M. I. *Appl. Catal., A* **1992**, *88* (1), 61−76.
(27) Palomino, R. M.; Magee, J. W.; Llorca, J.; Senanayake, S. D.; White, M. G. *J. Catal.* **2015**, *329*, 87−94.
(28) Yu, J.; Mao, D.; Han, L.; Guo, Q.; Lu, G. *J. Mol. Catal. A: Chem.* **2013**, *367*, 38−45.
(29) Zhou, S.; Zhao, H.; Ma, D.; Miao, S.; Cheng, M.; Bao, X. *Z. Phys. Chem.* **2005**, *219*, 949−961.
(30) Filot, I. A. W.; Shetty, S. G.; Hensen, E. J. M.; van Santen, R. A. *J. Phys. Chem. C* **2011**, *115* (29), 14204−14212.

(31) Wellendorff, J.; Lundgaard, K. T.; Møgelhøj, A.; Petzold, V.; Landis, D. D.; Nørskov, J. K.; Bligaard, T.; Jacobsen, K. W. *Phys. Rev. B: Condens. Matter Mater. Phys.* **2012**, *85* (23), 235149.

(32) Wellendorff, J.; Silbaugh, T. L.; Garcia-Pintos, D.; Nørskov, J. K.; Bligaard, T.; Studt, F.; Campbell, C. T. *Surf. Sci.* **2015**, *640*, 36−44.

(33) Studt, F.; Abild-Pedersen, F.; Varley, J. B.; Nørskov, J. K. *Catal. Lett.* **2013**, *143* (1), 71−73.

(34) Studt, F.; Behrens, M.; Kunkes, E. L.; Thomas, N.; Zander, S.; Tarasov, A.; Schumann, J.; Frei, E.; Varley, J. B.; Abild-Pedersen, F.; Nørskov, J. K.; Schlögl, R. *ChemCatChem* **2015**, *7* (7), 1105−1111.

(35) Medford, A. J.; Wellendorff, J.; Vojvodic, A.; Studt, F.; Abild-Pedersen, F.; Jacobsen, K. W.; Bligaard, T.; Nørskov, J. K. *Science* **2014**, *345*, 197−200.

(36) Giannozzi, P.; Baroni, S.; Bonini, N.; Calandra, M.; Car, R.; Cavazzoni, C.; Ceresoli, D.; Chiarotti, G. L.; Cococcioni, M.; Dabo, I.; Dal Corso, A.; de Gironcoli, S.; Fabris, S.; Fratesi, G.; Gebauer, R.; Gerstmann, U.; Gougoussis, C.; Kokalj, A.; Lazzeri, M.; Martin-Samos, L.; Marzari, N.; Mauri, F.; Mazzarello, R.; Paolini, S.; Pasquarello, A.; Paulatto, L.; Sbraccia, C.; Scandolo, S.; Sclauzero, G.; Seitsonen, A. P.; Smogunov, A.; Umari, P.; Wentzcovitch, R. M. *J. Phys.: Condens. Matter* **2009**, *21* (39), 395502.

(37) Monkhorst, H. J.; Pack, J. D. *Phys. Rev. B* **1976**, *13* (12), 5188−5192.

(38) Lee, K.; Murray, É. D.; Kong, L.; Lundqvist, B. I.; Langreth, D. C. *Phys. Rev. B: Condens. Matter Mater. Phys.* **2010**, *82* (8), 081101.

(39) Medford, A. J.; Sehested, J.; Rossmeisl, J.; Chorkendorff, I.; Studt, F.; Nørskov, J. K.; Moses, P. G. *J. Catal.* **2014**, *309*, 397−407.

(40) Brogaard, R.; Moses, P.; Nørskov, J. *Catal. Lett.* **2012**, *142* (9), 1057−1060.

(41) Bahn, S. R.; Jacobsen, K. W. *Comput. Sci. Eng.* **2002**, *4* (3), 56−66.

(42) Peterson, A. A. *Top. Catal.* **2014**, *57* (1), 40−53.

(43) Koskinen, P.; Mäkinen, V. *Comput. Mater. Sci.* **2009**, *47* (1), 237−253.

(44) Henkelman, G.; Uberuaga, B. P.; Jónsson, H. *J. Chem. Phys.* **2000**, *113* (22), 9901.

(45) Brogaard, R. Y.; Henry, R.; Schuurman, Y.; Medford, A. J.; Moses, P. G.; Beato, P.; Svelle, S.; Nørskov, J. K.; Olsbye, U. *J. Catal.* **2014**, *314*, 159−169.

(46) Shomate, C. H. *J. Phys. Chem.* **1954**, *58* (4), 368−372.

(47) Medford, A. J.; Shi, C.; Hoffmann, M. J.; Lausche, A. C.; Fitzgibbon, S. R.; Bligaard, T.; Nørskov, J. K. *Catal. Lett.* **2015**, *145*, 794−807.

(48) Lausche, A. C.; Medford, A. J.; Khan, T. S.; Xu, Y.; Bligaard, T.; Abild-Pedersen, F.; Nørskov, J. K.; Studt, F. *J. Catal.* **2013**, *307*, 275−282.

(49) Mavrikakis, M.; Bäumer, M.; Freund, H. J.; Nørskov, J. K.; Ba, M. *Catal. Lett.* **2002**, *81*, 153−156.

(50) Hammer, B.; Hansen, L. B.; Nørskov, J. K. *Phys. Rev. B: Condens. Matter Mater. Phys.* **1999**, *59* (11), 7413−7421.

(51) Tüshaus, M.; Berndt, W.; Conrad, H.; Bradshaw, A. M.; Persson, B. *Appl. Phys. A: Solids Surf.* **1990**, *51* (2), 91−98.

(52) Sangwal, K. *J. Cryst. Growth* **1999**, *203*, 197−212.

(53) Bengaard, H. S.; Nørskov, J. K.; Sehested, J.; Clausen, B. S.; Nielsen, L. P.; Molenbroek, A. M.; Rostrup-Nielsen, J. R. *J. Catal.* **2002**, *209* (2), 365−384.

(54) Somarjai, G. A.; Garfunkel, E. L. *Mater. Sci. Monogr.* **1989**, *57*, 319−330.

(55) Luo, H. Y.; Lin, P. Z.; Xie, S. B.; Zhou, H. W.; Xu, C. H.; Huang, S. Y.; Lin, L. W.; Liang, D. B.; Yin, P. L.; Xin, Q. *J. Mol. Catal. A: Chem.* **1997**, *122* (2), 115−123.

(56) Schwartz, V.; Campos, A.; Egbebi, A.; Spivey, J. J.; Overbury, S. H. *ACS Catal.* **2011**, *1* (10), 1298−1306.

(57) Chuang, S. C.; Goodwin, J. G.; Wender, I. *J. Catal.* **1985**, *92* (2), 416−421.

(58) Hu, J.; Wang, Y.; Cao, C.; Elliott, D. C.; Stevens, D. J.; White, J. F. *Catal. Today* **2007**, *120* (1), 90−95.

(59) Orita, H.; Naito, S.; Tamaru, K. *J. Catal.* **1984**, *90*, 183−193.

(60) Hanaoka, T.; Arakawa, H.; Matsuzaki, T.; Sugi, Y.; Kanno, K.; Abe, Y. *Catal. Today* **2000**, *58* (4), 271−280.